

Banner appropriate to article type will appear here in typeset article

Multiple states of two-dimensional turbulence above topography

Jiyang He^{1,2} and Yan Wang^{1,2}†

¹Department of Ocean Science, The Hong Kong University of Science and Technology, Hong Kong, China

²Center for Ocean Research in Hong Kong and Macau, The Hong Kong University of Science and Technology, Hong Kong, China.

(Received xx; revised xx; accepted xx)

The recent work of Siegelman & Young (PNAS, vol. 120(44), 2023, pp. e2308018120) revealed two extreme states reached by the evolution of unforced and weakly-damped two-dimensional turbulence above random rough topography, separated by a critical kinetic energy $E_{\#}$. The low- and high-energy solutions correspond to topographically-locked and roaming vortices, surrounded by non-uniform and homogeneous background potential vorticity (PV), respectively. However, we found that these phenomena are restricted to the particular intermediate length scale where the energy was initially injected into the system. Through simulations initialised by injecting the energy at larger and smaller length scales, we found that the long-term state of topographic turbulence is also dependent on the initial length scale. If the initial length scale is comparable with the domain size, the flow field evolves to the minimum-ensrophy state proposed by Bretherton and Haidvogel (J. Fluid Mech., vol.78(1), 1976, pp. 129-154), without the presence of vortices, especially when the energy is no larger than $E_{\#}$. As the initial length scale becomes smaller, more vortices nucleate, and become more mobile. Simultaneously, the background PV tends to homogenization, even if the energy is below $E_{\#}$. These results complement the phenomenology of topographic turbulence documented by Siegelman & Young, by showing that the minimum-ensrophy and background PV homogenization states can be reached by large- and small-scale initial fields, respectively, whatever the energy is.

Key words:

1. Introduction

Two-dimensional, rapidly-rotating turbulence above topography (topographic turbulence hereafter) serves as an effective reduced model for studying large-scale oceanic motions over rough and sloping seafloor. This model has provided insight into the emergence of prevailing undercurrents over continental shelves and slopes (Wang & Stewart 2018) and persistent along-bathymetry flows above topographic depressions and seamounts (Solodoch

† Email address for correspondence: yanwang@ust.hk

et al. 2021). Topographic turbulence is also relevant to long-lived, anticyclonic vortices locked to large-scale topographic bowls in the ocean, such as the Lofoten Basin Eddy and the Mann Eddy in the North Atlantic (see Köhl 2007; LaCasce *et al.* 2024). Since current climate models remain to fall short of resolving turbulent flows in the ocean, employing the topographic turbulence model to investigate phenomena arising from it will facilitate the parameterization of ocean turbulence over bumpy seabeds in these models (Holloway 1992; Radko 2023; Eaves *et al.* 2024).

Theories of topographic turbulence aimed to derive the steady states via variational principles. For an energy-conserving system, the potential enstrophy is minimized (Bretherton & Haidvogel 1976), leading to a linear relation between the potential vorticity (PV hereafter) and geostrophic streamfunction. The other approach is to maximize the entropy and is thus related to the equilibrium statistical mechanics (Salmon *et al.* 1976). The ensembles of PV and streamfunction also satisfy a linear relation. According to Carnevale & Frederiksen (1987), the two solutions are actually consistent with each other, and nonlinearly stable.

Recent numerical experiments show that topographic turbulence shares some common features with flat-bottom two-dimensional turbulence (2DT). For instance, condensed states commonly found in 2DT (Boffetta & Ecke 2012) have been identified in topographic turbulence over small-scale topography (Zhang & Xie 2023; Gallet 2024). Siegelman & Young (2023) (SY23 hereafter) showed the coexistence of vortices and a background flow in topographic turbulence, the former of which are prevalent in 2DT (McWilliams 1984, 1990). They found that the mobility of vortices and the uniformity of background flows depend on the energy of the system: on the low-energy branch, the vortices are locked to topographic features, and the background PV is spatially non-uniform; on the high-energy branch, the vortices roam throughout the domain, and the background PV is homogenized (Rhines & Young 1982). These two branches are separated by a critical energy.

SY23 examined the minimum-*enstrophy* hypothesis of Bretherton & Haidvogel (1976) against their numerical simulations, and identified significant discrepancies: the high-energy solutions displayed homogeneous background PV that is not predicted by the minimum-*enstrophy* hypothesis at the same high energy; the long-term total *enstrophy* far exceeded that of the theoretical prediction for almost all energies. SY23 attributed these discrepancies to the presence of long-lived vortices: the roaming of vortices mixes the background PV toward homogeneity, and vortex shielding inhibits *enstrophy* from cascading to smaller scales.

In this work, we will show that the emergence of vortices might relate to the specific intermediate length scale of the initial fields prescribed by SY23, at which the initial total *enstrophy* is much higher than the theoretical minimum value and the large margin may serve as the seeds of vortices. As opposed to fixing an initially energized wavenumber, we conduct numerical experiments similar to those of SY23 but initialised by monoscale fields sweeping a broad range of wavenumbers, from scales comparable to the domain size to those much smaller than that chosen by SY23. The purpose here is to investigate how topographic turbulence evolves in response to different scales of initial conditions: can the emergence of vortices be inhibited and the minimum-*enstrophy* state be reached if the initial scale is adequately large; what would occur if the initial scale is smaller than that of SY23?

2. Framework

2.1. Theory

As in SY23, we consider an unforced, single-layer quasi-geostrophic (QG) flow on a f -plane in a doubly-periodic domain ($L \times L$, with L denoting the domain size). The governing

equation of the QG PV $q(x, y, t)$ reads

$$\frac{\partial q}{\partial t} + \frac{\partial \psi}{\partial x} \frac{\partial q}{\partial y} - \frac{\partial \psi}{\partial y} \frac{\partial q}{\partial x} = D\zeta, \quad q = \zeta + \eta = \nabla^2 \psi + \eta, \quad (2.1a, b)$$

where ψ and ζ are the geostrophic streamfunction and relative vorticity, respectively. The operator D stands for the dissipation of PV that will be specified later. Effects from bottom topography are encoded in the topographic PV, $\eta(x, y) = -f_0 h_1 / h_0$, for a total depth of $h_0 + h_1(x, y)$ with small fluctuations $h_1(x, y)$ around a constant average h_0 , scaled by the local Coriolis frequency f_0 (see SY23).

In the absence of dissipation, the system (2.1) conserves the kinetic energy and total enstrophy, defined respectively as

$$E = \frac{1}{2} \langle |\nabla \psi|^2 \rangle = \frac{1}{2L^2} \iint |\nabla \psi|^2 dx dy \quad \text{and} \quad Q = \frac{1}{2} \langle q^2 \rangle = \frac{1}{2L^2} \iint q^2 dx dy. \quad (2.2a, b)$$

Here $\langle \cdot \rangle$ represents an domain-average operation. When the added dissipation in the governing equation (2.1) operates at high wavenumbers, the energy is approximately conserved, while the enstrophy drops by a large amount as a result of forward cascade. This motivated Bretherton & Haidvogel (1976) to predict that an energy-conserving system would evolve into a minimum-enstrophy state. The state can be obtained by performing variational calculation of the functional $\mathcal{L} = Q + \mu E$, with μ denoting the Lagrange multiplier. The resulting Euler-Lagrange equation,

$$q_* = \nabla^2 \psi_* + \eta = \mu \psi_*, \quad (2.3)$$

dictates a linear relation between q_* and ψ_* . Solutions to (2.3) are actually inviscid steady solutions to the QG PV equation (2.1).

To solve the equation (2.3), the topographic PV can be Fourier-transformed into

$$\eta(x, y) = \sum_{\mathbf{k}} \eta_{\mathbf{k}} e^{i\mathbf{k} \cdot \mathbf{x}}, \quad (2.4)$$

where \mathbf{k} represents the wavenumber vector. As in SY23, the topographic PV is chosen to satisfy a power spectrum of k^{-2} ($k = |\mathbf{k}|$), by which the Fourier amplitudes in the expression (2.4) shall take the form

$$\eta_{\mathbf{k}} = \alpha e^{i\phi_{\mathbf{k}}} k^{-3/2}. \quad (2.5)$$

The normalization parameter α is adjusted to produce a specific value of the root mean square of the topographic PV, defined as $\eta_{rms} = \sqrt{\sum_{\mathbf{k}} |\eta_{\mathbf{k}}|^2}$. Following SY23, we prescribe $\eta_{rms} = 10^{-6} \text{ s}^{-1}$. Meanwhile, the random phase $\phi_{\mathbf{k}}$ in (2.5) serves to produce a realization of η . Throughout this work, the topography remains fixed, and is shown in figure 1.

With the prescribed topography, the solution to the Euler-Lagrange equation (2.3) can be obtained in spectral space as

$$\psi_*(x, y, \mu) = \sum_{\mathbf{k}} \frac{\eta_{\mathbf{k}} e^{i\mathbf{k} \cdot \mathbf{x}}}{\mu + k^2}. \quad (2.6)$$

The corresponding energy and minimum enstrophy are then

$$E = \frac{1}{2} \sum_{\mathbf{k}} \frac{k^2 |\eta_{\mathbf{k}}|^2}{(\mu + k^2)^2} \quad \text{and} \quad Q_{min} = \frac{1}{2} \sum_{\mathbf{k}} \frac{\mu^2 |\eta_{\mathbf{k}}|^2}{(\mu + k^2)^2}, \quad (2.7a, b)$$

respectively. With a given energy level E for an energy-conserving system, the Lagrange multiplier μ and minimum enstrophy Q_{min} can be sought through the above relations.

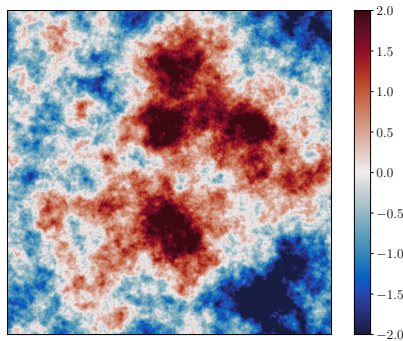


Figure 1: Topographic potential vorticity $\eta(x, y)$ (unit : 10^{-6} s^{-1}) used throughout this work.

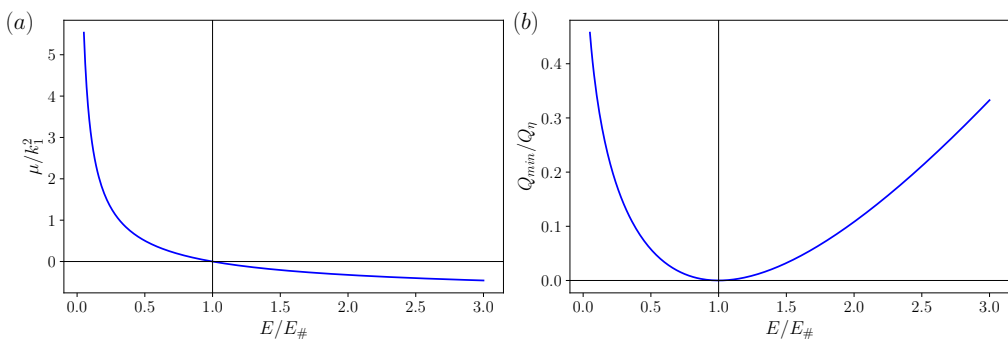


Figure 2: Minimum-entropy solutions as in SY23 (see their Figures 2(a)–(b)).

Figure 2(a, b) show the resulting μ and Q_{min} as functions of E , respectively, scaled by k_1^2 ($k_1 = 2\pi/L$ represents the fundamental wavenumber) and $Q_\eta = \eta_{rms}^2/2$. In addition, the energy has been scaled by the critical energy level $E_\#$, corresponding to the particular case of $\mu = 0$ and thus of homogenized PV ($q_\# = 0$). At this critical energy, the minimum enstrophy vanishes ($Q_{min} = 0$; see figure 2(b)). The critical energy $E_\#$ separates the low- and high-energy branches, which correspond to positive and negative values of μ , respectively. These theoretical solutions are identical to those shown in SY23 (see their figure 2(a, b)), who further found that $E_\#$ is a good separator of high- and low-energy branches of their numerical experiments.

2.2. Numerical setups

We solve the QG PV equation (2.1) using the open-source pseudo-spectral package *GeophysicalFlows.jl* running on GPUs (Constantinou *et al.* 2021). Time is stepped forward by a fourth-order Rounge-Kutta scheme. The dissipation term ($D\zeta$) in (2.1) is implemented via a spectral filter of relative vorticity, which is applied to high wavenumbers at the end of each time step. We choose exactly the same parameter setups as in SY23: the domain size is 10^6 meters; the resolution is 1024×1024 ; the integration time is 1.5×10^9 seconds (around 47.53 years); time step is 1500 seconds, which is reduced further to 500 seconds for computationally demanding runs.

We initialise the computations by a series of random monoscale relative vorticity fields with a wide range of enstrophy, which is achieved by different combinations of the wavenumber and energy level. For all cases, the Fourier components of the initial relative vorticity $\zeta(x, y, 0)$

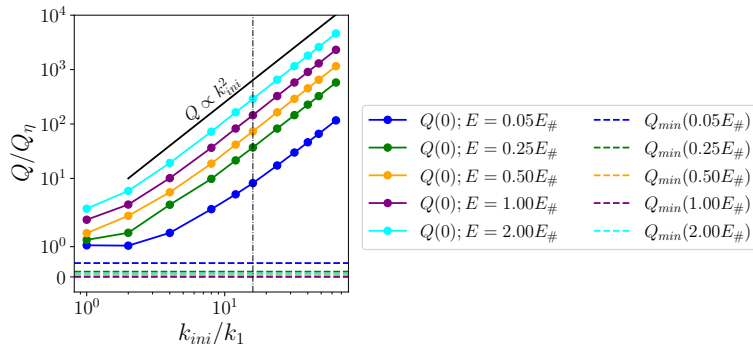


Figure 3: Variations of initial entrophy $Q(0)$ with the initial wavenumber k_{ini} for different energies, compared with the minimum entrophy Q_{min} .

are chosen randomly within the bandwidth $[k_{ini} - 0.5k_1, k_{ini} + 0.5k_1]$, where k_{ini} is the wavenumber of the initial monoscale field. In practice, we choose a series of

$$k_{ini} \in \{1, 2, 4, 8, 12, 16, 24, 32, 48, 64\}k_1, \quad (2.8)$$

corresponding to large-to-small initial monoscales, and

$$E \in \{0.05, 0.25, 0.50, 1.00, 2.00\}E_{\#}, \quad (2.9)$$

corresponding to low-to-high energy levels. Note that SY23 prescribed the initial monoscale at approximately $16k_1$, which is intermediate in our selected range of wavenumbers (2.8). The initial entrophy for different combinations of k_{ini} and E is shown in figure 3, estimated as $Q(0) \approx k_{ini}^2 E + Q_{\eta}$. That is, with a prescribed energy level, $Q(0)$ increases at a rate of k_{ini}^2 , which means that the larger amount of initial entrophy is contained at the smaller scales. As shown in figure 3, the initial entrophy exceeds the theoretical minimum entrophy for all cases. However, the former is adequately close to the latter in the small- k_{ini} regime, as opposed to the case of intermediate wavenumber (highlighted by the vertical dotted-dashed line in figure 3) considered by SY23. Owing to the initial/minimum entrophy proximity, small- k_{ini} runs may readily converge to the minimum-entrophy states.

3. Results

In this section, we analyse the solutions of our numerical experiments. Particular attention is paid to the dependence of the long-term state on the initial wavenumber k_{ini} . Results of $k_{ini} = 16k_1$, consistent with those in SY23, are highlighted in red color upon comparison with other wavenumber cases.

3.1. Time evolution of energy and entrophy

The time evolution of energy and entrophy is shown in figure 4 for simulations of the critical energy $E/E_{\#} = 1$ (results of other energies exhibit similar behaviours and are not shown). As shown in figure 4(a), the energy loss during run time is larger for larger k_{ini} , because the corresponding initial spectral position of energy injection is closer to the filtering region at high wavenumbers. However, the energy loss at the final time (47.53 years) amounts to a negligible fraction of the initial energy, within 0.3% for $k_{ini} \leq 16k_1$ and around 3% for $k_{ini} = 64k_1$ (see first column of numbers in table 1). Therefore, energy is nearly conserved for all runs, which is the necessary condition for examining the minimum-entrophy hypothesis.

By contrast, the entrophy decreases drastically during run time, as shown in figure 4(b).

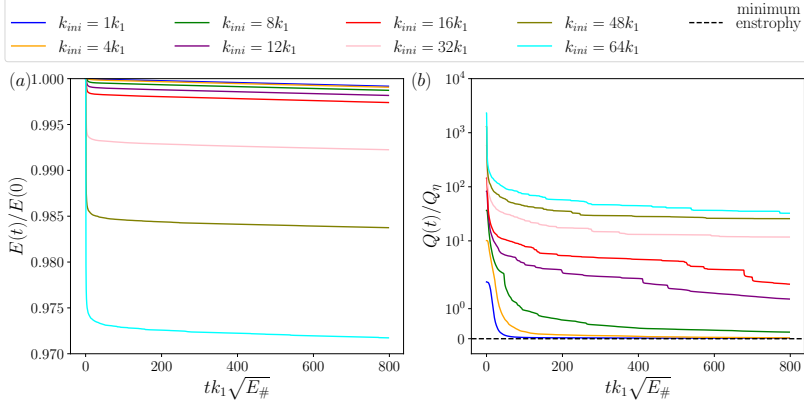


Figure 4: Time evolution of energy (a) and enstrophy (b) for the $E_\#$ runs.

$k_{ini} \backslash E$	$0.05E_\#$	$0.25E_\#$	$0.50E_\#$	$E_\#$	$2E_\#$
theory	1.000; 0.457	1.000; 0.174	1.000; 0.057	1.000; 0.000	1.000; 0.108
$1k_1$	0.997; 0.465	0.999; 0.177	0.999; 0.061	0.999; 0.017	0.999; 0.193
$2k_1$	0.997; 0.472	0.999; 0.184	0.999; 0.064	0.999; 0.006	0.999; 0.299
$4k_1$	0.997; 0.475	0.998; 0.181	0.999; 0.092	0.999; 0.030	0.999; 2.105
$8k_1$	0.997; 0.468	0.998; 0.224	0.998; 0.323	0.999; 0.220	0.999; 2.420
$12k_1$	0.996; 0.480	0.998; 0.605	0.998; 1.173	0.998; 1.321	0.998; 5.238
$16k_1$	0.996; 0.582	0.997; 1.305	0.997; 2.081	0.997; 1.816	0.998; 8.734
$32k_1$	0.990; 1.170	0.992; 3.835	0.992; 5.766	0.992; 11.76	0.992; 20.98
$48k_1$	0.981; 2.022	0.983; 6.945	0.983; 9.439	0.984; 25.73	0.984; 36.76
$64k_1$	0.969; 3.115	0.971; 11.12	0.971; 16.50	0.972; 32.41	0.972; 63.38

Table 1: Energy $E(47.53 \text{ years})/E(0)$ (first column of numbers) and enstrophy $Q(47.53 \text{ years})/Q_\eta$ (second column of numbers) for runs with different k_{ini} and E , compared against the theoretical predictions (first row).

Consistent with the findings of SY23, there is an initial fast drop followed by a slow decrease. Generally, for a fixed energy level, larger- k_{ini} runs, or equivalently, runs with higher initial enstrophy (see figure 3), maintain higher enstrophy during run time. Runs with small k_{ini} are intriguing: the enstrophy approaches the minimum value Q_{min} during run time. At the final time (see second column of numbers in table 1), the enstrophy Q of small- k_{ini} ($1k_1$, $2k_1$, $4k_1$) runs prescribed with low energy ($E/E_\# \leq 1$) is extremely close to the corresponding minimum value Q_{min} . However, for the high energy case of $2E_\#$, the final enstrophy of the $1k_1$ run is almost twice the minimum value. For the intermediate case of $k_{ini} = 16k_1$ considered by SY23 and cases with larger k_{ini} , the final enstrophy is much larger than the minimum value, except for the lowest-energy runs ($0.05E_\#$). Thus, the minimum-enstrophy states can actually be reached by runs with large-scale initial conditions, especially by those with low energy ($E/E_\# \leq 1$). These findings contrast markedly with the conclusions of SY23.

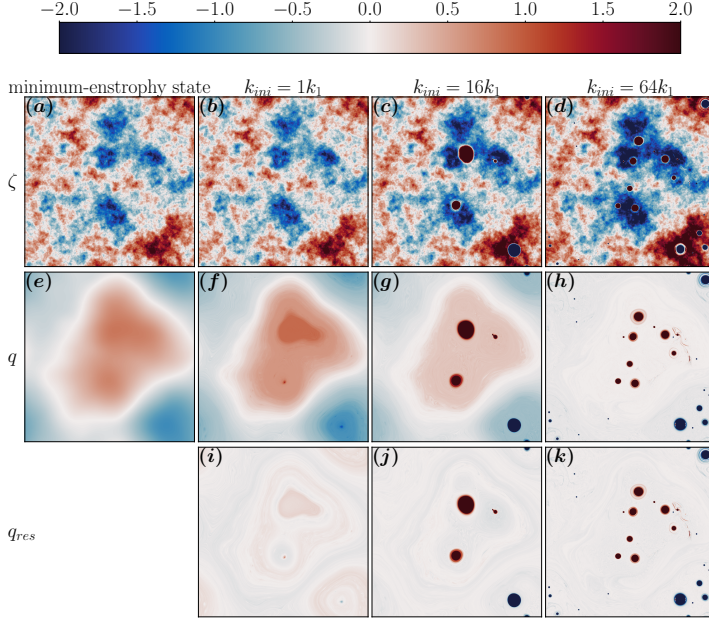


Figure 5: Long-term snapshots of $0.25E_{\#}$ runs for $k_{ini} = [1, 16, 64]k_l$ (second-fourth columns) compared with the minimum-entropy state at the same energy level (first column): first row, ζ ; second row, q ; third row, q_{res} .

3.2. Long-term states

Next we inspect the long-term snapshots in runs with typical energy levels at the final time (47.53 years), and compare those with the minimum-entropy states ζ_* and q_* obtained theoretically. The corresponding animations, showing the time evolution to the long-term states, can be found in the supplementary materials.

Figure 5 compares the snapshots of relative vorticity (first row) and PV (second row) from three runs with different k_{ini} against the minimum-entropy states ζ_* and q_* obtained theoretically. The state of the smallest $k_{ini} = 1k_l$ run (figure 5(b, f)) resembles the minimum-entropy state (figure 5(a, e)), displaying a non-uniform PV field shaped by the low-pass-filtered topography throughout the domain. This resemblance is consistent with the proximity of the corresponding entropy (see table 1), and further demonstrates that the minimum-entropy state can actually be reached with very large-scale initial conditions. However, although no strong vortices emerge, there exist some weak extrema of PV (see figure 5(f)) at the topographic depressions and elevations (see figure 1 for topography). As k_{ini} increases to $16k_l$, strong vortices emerge at these locations, with cyclones and anticyclones locked to topographic elevations and depressions, respectively (figure 5(g)). The background relative vorticity becomes stronger (compare figure 5(c) with (b)), leading to the weaker background PV (compare figure 5(g) with (f)). As k_{ini} increases further to $64k_l$, more vortices show up. Notably, the background relative vorticity strengthens further and the background PV is nearly homogenized (figure 5(d, h)). A larger initial wavenumber provides more seeds of vortices; more vortices nucleate afterwards and mix the background PV more efficiently to homogeneity. Note that the vortices in the $64k_l$ run remain locked to fixed locations but exhibit higher mobility compared to those in the $16k_l$ run (see supplementary movies of the corresponding runs). In summary, at a low energy level, the resemblance with the minimum-entropy state and the near homogenization of background PV are observed in

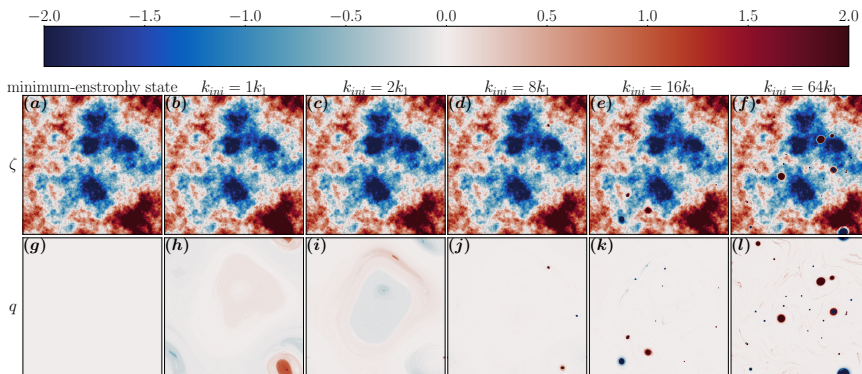


Figure 6: Long-term snapshots of $E_{\#}$ runs for $k_{ini} = [1, 2, 8, 16, 64]k_1$ (second-sixth columns) compared with the minimum entrophy state at the same energy level (first column): first row, ζ ; second row, q .

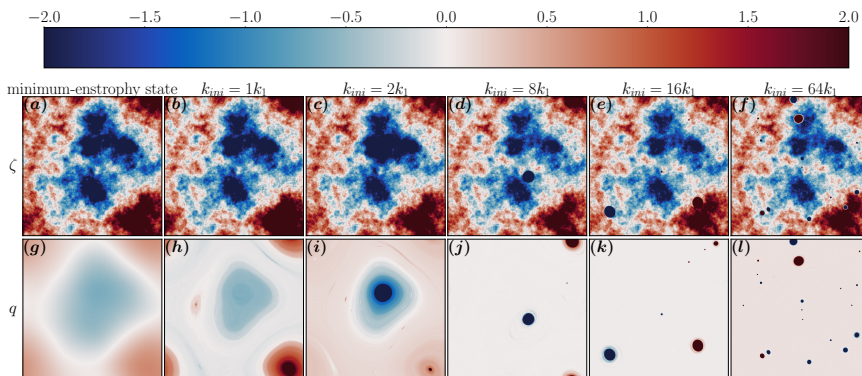


Figure 7: Same as figure 6 but for $2E_{\#}$ runs.

simulations with two limiting initial length scales, with an emergent transitional state as the initial length scale varies in between. These phenomena cannot be observed in low-energy simulations with a single intermediate wavenumber of $16k_1$ considered by SY23.

Now we turn to the runs with the critical energy level of $E_{\#}$, as shown in figure 6. Once again, the solutions of the small- k_{ini} runs are similar to the minimum-entrophy state, with nearly homogenized PV (see figure 6(h,i)). This demonstrates that the minimum-entrophy state can be reached, together with the analogous entrophy produced numerically and theoretically (table 1). As k_{ini} increases, more vortices nucleate and roam throughout the domain. The background PV is then completely homogenized.

A parallel comparison is made further among simulations prescribed with the high energy level of $2E_{\#}$, shown in figure 7. As discussed earlier, the final-state entrophy does not approach the minimum value, even for the case of the smallest initial wavenumber $1k_1$ (table 1). However, the solution of the $1k_1$ run is still similar to the minimum entrophy state to some extent (figure 7(g,h)), both displaying non-uniform PV fields imprinted by the low-pass-filtered topography. However, as shown in figure 7(h,i) for runs of $1k_1$ and $2k_1$, a cyclone and an anticyclone are locked respectively to the topographic depression and elevation, exactly opposing the relation between vortex polarity and depth in the low-energy runs. These gigantic vortices inhibit entrophy from further decaying toward the theoretical minimum value. Toward the case of $8k_1$, the vortices become smaller in size and more

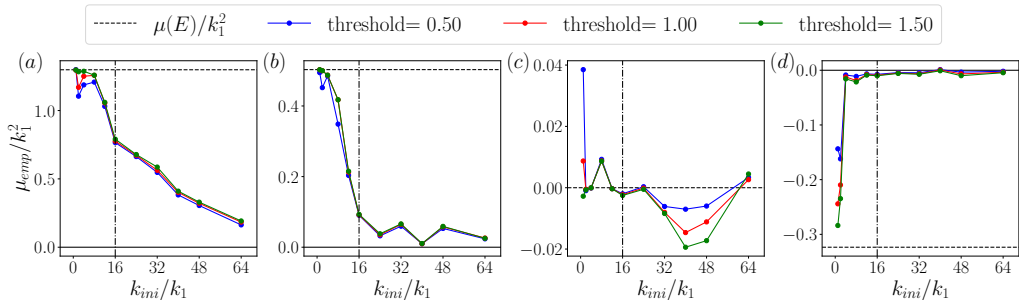


Figure 8: Variations of the empirical slope μ_{emp} between q and ψ with the initial wavenumber k_{ini}/k_1 at four energy levels: (a) $E = 0.25E_{\#}$; (b) $E = 0.50E_{\#}$; (c) $E = E_{\#}$; (d) $E = 2E_{\#}$. Horizontal dashed lines represent the theoretical Lagrange multiplier based on the minimum-entropy principle at the same energy levels. Vertical dotted-dashed lines highlight the wavenumber of $k_{init}/k_1 = 16$ considered in SY23.

localised; they orbit around the large-scale features of topography (see the corresponding supplementary movie). The background PV is essentially homogenized. As k_{ini} increases further, more vortices emerge and tend to roam throughout the domain. Note that, although the background PV of the $64k_1$ run is homogenized, it is not identically zero.

3.3. Empirical background flow

As in SY23, we extract the background flow from the data via linear fitting between q and ψ . The vortices in the flow field are outliers and removed by a threshold. The points with $|q|/\eta_{rms}$ below the threshold are retained to extract the background state. Then applying least-squares fitting to q and ψ of the remaining points yields an approximate linear relation,

$$q \approx \mu_{emp}\psi. \quad (3.1)$$

When extracting the empirical slope μ_{emp} for each time instant, we found that its value does not vary significantly in time after an initial adjustment phase. The empirical slope μ_{emp} should depend on the energy E , as illustrated by SY23, and the initial wavenumber k_{ini} based on our experiments. The results of μ_{emp} are shown in figure 8. We choose three thresholds for extracting μ_{emp} , and find only quantitative differences. The runs with the critical energy $E_{\#}$ show that μ_{emp} is always close to zero, indicating near PV homogenization. For small- k_{ini} runs, the empirical slope μ_{emp} is close to the theoretical $\mu(E)$ (horizontal dashed line) shown in figure 2(a). Even at the high energy level of $2E_{\#}$, a negative μ_{emp} is consistent with the theoretical $\mu(2E_{\#})$. This is another justification of the existence of the minimum entropy state achievable by numerical simulations but not obtained by SY23. As the initial wavenumber increases, the magnitude of μ_{emp} tends to zero, implying a transition from a non-uniform background PV field imprinted by the low-pass-filtered topography to PV homogenization, consistent with the preceding observations from the long-term snapshots. The numerical solutions of SY23 (see vertical dotted-dashed lines) might capture a confined range of the transition regime, particularly in the low-energy cases.

As in SY23, the empirical slope μ_{emp} is used to define a “residual” PV field, $q_{res} = q - \mu_{emp}\psi$, which is shown in figure 5(i, j, k). Evidently, the background flow is sufficiently removed, thus confirming the q - ψ linear relation (3.1).

4. Conclusion

In this work, we study the states of unforced, weakly-decaying two-dimensional turbulence above random rough topography, initialised by a series of monoscale fields covering a broad range of length scales and energy levels. Our observations complement those of Siegelman & Young (2023), who took a single, intermediate monoscale for initialisation into account. Some of the phenomenological descriptions of topographic turbulence from Siegelman & Young (2023) shall be updated. The minimum-entropy solutions of Bretherton & Haidvogel (1976) can be reached by initial fields whose length scales are comparable with the domain size, especially when the energy is no larger than $E_{\#}$. As the initial length scale decreases, the higher initial enstrophy provides more seeds for vortex nucleation. More emerging vortices shield enstrophy from cascading toward high wavenumbers, and efficiently mix the background PV. A non-uniform background PV field imprinted by large-scale topography, at low or high energy, is thus weakened and tends to homogenization. Our results highlight the sensitivity of topographic turbulence to the length scales of initial conditions. Given that the depth-invariant mode of geostrophic turbulence responsible for driving mass and heat transports was constantly found to be energized across a range of wavenumbers (Chen 2023), this work calls for ongoing efforts for refining parameterisations of ocean turbulence over bumpy seafloor by taking the energization length scales into account.

Acknowledgements. This work is supported by the Research Grants Council (RGC) of Hong Kong under awards Early Career Scheme 26307720 and General Research Fund 16305321, and by the Center for Ocean Research (CORE), a joint research center between Laoshan Laboratory and HKUST.

Declaration of interests. The authors report no conflict of interest.

REFERENCES

- BOFFETTA, G. & ECKE, R. E. 2012 Two-Dimensional Turbulence. *Annu. Rev. Fluid Mech.* **44** (1), 427–451.
- BREThERTON, F. P. & HAIDVOGEL, D. B. 1976 Two-dimensional turbulence above topography. *J. Fluid Mech.* **78** (1), 129–154.
- CARNEVALE, G. F. & FREDERIKSEN, J. S. 1987 Nonlinear stability and statistical mechanics of flow over topography. *J. Fluid Mech.* **175** (-1), 157.
- CHEN, S.-N. 2023 Revisiting the baroclinic eddy scalings in two-layer, quasigeostrophic turbulence: Effects of partial barotropization. *J. Phys. Oceanogr.* **53** (3), 891 – 913.
- CONSTANTINOU, NAVID C., WAGNER, GREGORY LeCLAIRE, SIEGELMAN, LIA, PEARSON, BRODIE C. & PALÓCZY, ANDRÉ 2021 GeophysicalFlows.jl: Solvers for geophysical fluid dynamics problems in periodic domains on CPUs & GPUs. *J. Open Source Softw.* **6** (60), 3053.
- EAVES, R. E., MADDISON, J. R., MARSHALL, D. P. & WATERMAN, S. 2024 An energy and enstrophy constrained parameterization of barotropic eddy potential vorticity fluxes. Preprint. Preprints.
- GALLET, B. 2024 Two-dimensional turbulence above topography: Condensation transition and selection of minimum enstrophy solutions, arXiv: 2404.06475.
- HOLLOWAY, G. 1992 Representing Topographic Stress for Large-Scale Ocean Models. *J. Phys. Oceanogr.* **22** (9), 1033–1046.
- KÖHL, A. 2007 Generation and Stability of a Quasi-Permanent Vortex in the Lofoten Basin. *J. Phys. Oceanogr.* **37** (11), 2637–2651.
- LACASSE, J. H., PALÓCZY, A. & TRODAHL, M. 2024 Vortices over bathymetry. *J. Fluid Mech.* **979**, A32.
- MCWILLIAMS, J. C. 1984 The emergence of isolated coherent vortices in turbulent flow. *J. Fluid Mech.* **146**, 21–43.
- MCWILLIAMS, J. C. 1990 The vortices of two-dimensional turbulence. *J. Fluid Mech.* **219** (-1), 361.
- RADKO, T. 2023 A generalized theory of flow forcing by rough topography. *J. Fluid Mech.* **961**, A24.
- RHINES, P. B. & YOUNG, W. R. 1982 Homogenization of potential vorticity in planetary gyres. *J. Fluid Mech.* **122** (-1), 347.
- SALMON, R., HOLLOWAY, G. & HENDERSHOTT, M. C. 1976 The equilibrium statistical mechanics of simple quasi-geostrophic models. *J. Fluid Mech.* **75** (4), 691–703.

- SIEGELMAN, L. & YOUNG, W. R. 2023 Two-dimensional turbulence above topography: Vortices and potential vorticity homogenization. *PNAS* **120** (44), e2308018120.
- SOLODOCH, A., STEWART, A. L. & McWILLIAMS, J. C. 2021 Formation of Anticyclones above Topographic Depressions. *J. Phys. Oceanogr.* **51** (1), 207–228.
- WANG, Y. & STEWART, A. L. 2018 Eddy dynamics over continental slopes under retrograde winds: Insights from a model inter-comparison. *Ocean Model.* **121**, 1–18.
- ZHANG, L.-F. & XIE, J.-H. 2023 Spectral condensation in quasi-geostrophic turbulence above small-scale topography, arXiv: 2311.16612.